Interaction potentials for two-particle states with nonzero total momenta in lattice QCD

Yutaro Akahoshi[*] and Sinya Aoki

Center for Gravitational Physics, Yukawa Institute for Theoretical Physics Kyoto University,
Kyoto 606-8502, Japan
and RIKEN Nishina Center (RNC), Saitama 351-0198, Japan

In this study, we extend the HAL QCD method to a case where a total momentum of a two-particle system is nonzero and apply it to the $I = 2$ S-wave $\pi\pi$ scattering in order to confirm its validity. We derive a fundamental relation of an energy-independent nonlocal potential defined in the center of mass frame with Nambu-Bethe-Salpeter wave functions in a laboratory frame. Based on the relation, we propose the time-dependent method to extract potentials, often used in practice for the HALQCD method in the center of mass frame. For numerical simulations in the $I = 2$ $\pi\pi$ system, we employ $(2 + 1)$-flavor gauge configurations on a $32^3 \times 64$ lattice at the lattice spacing $a \approx 0.0907$ fm and $m_\pi \approx 700$ MeV. Both effective leading order (LO) potentials and corresponding phase shifts obtained in laboratory frames agree with those obtained in the center-of-mass frame by the conventional HAL QCD method within somewhat larger statistical errors. In addition, we observe a consistency in scattering phase shifts between ours and results by the finite-volume method as well. The HAL QCD method with nonzero total momenta, established in this study, brings more flexibility to the HAL QCD method, which enables us to handle systems having the same quantum numbers with a vacuum or to access energy regions prohibited in the center of mass frame.

I. INTRODUCTION

A first-principle determination of hadron interactions in quantum chromodynamics (QCD) is one of the most important challenges for understanding the nature of hadronic resonances observed in experiments. In recent years, hadron interactions have been actively studied in lattice QCD by employing two methods: the finite-volume method [1–3] and the HAL QCD method [4–7]. Theoretically, both methods rely on the Nambu-Bethe-Salpeter (NBS) wave function, which links to the scattering S matrix in QCD. The finite-volume method gives a formula relating finite-volume energy spectra to scattering phase shifts in the infinite volume, by considering behaviors of NBS wave functions in an asymptotic region. In the HAL QCD method, on the other hand, one directly extracts energy-independent nonlocal potentials through spatial

dependences of NBS wave functions in an interacting region and then calculates scattering phase shifts by solving Schrödinger equations with these potentials in the infinite volume. Armed with the time-dependent method [7] and the multichannel extension [8], the HAL QCD method has been successfully applied to two-baryon systems with various pion masses (see Ref. [9] and references therein for the recent status). Recently, resonance studies such as the ρ meson have become possible thanks to rapid improvements in calculation techniques of all-to-all quark propagators [10–13].

In the finite-volume method, not only the center of mass frame but also laboratory frames with nonzero total momenta [2] are employed for calculations of two hadron spectra, in order to access different finite-volume energies as many as possible for a given volume, which provide energy dependences of scattering observables precise enough for determinations of resonance parameters [14,15].

In the HAL QCD method, on the other hand, all calculations so far have been made in the center of mass frame, since the time-dependent HAL QCD method [7] does not require isolation of an energy eigenstate but utilizes all elastic states below inelastic thresholds at some degree. The recent ρ resonance study, however, reveals that P-wave scattering phase shifts can not be determined

precisely in a low-energy region not accessible in the center-of-mass frame due to nonzero relative momenta of the P wave [16]. Thus, the HAL QCD method in laboratory frames with nonzero momenta will provide a better alternative for a more precise determination of P-wave scatterings. In addition, the HAL QCD method in laboratory frames is mandatory to investigate hadron resonances having the same quantum numbers with a vacuum such as the $I = 0$ S-wave $\pi\pi$ interaction corresponding to the σ resonance, since a large mixing to a vacuum state in the center of mass frame is much reduced in a laboratory frame.

An extraction of HAL QCD potentials using laboratory frames with nonzero total momenta has been theoretically formulated and briefly reported in [17]. Applications of the method to hadron systems in lattice QCD, however, require numerically demanding calculations of all-to-all quark propagators, which are employed to construct appropriate source operators with nonzero total momenta. As already mentioned, recent algorithmic improvements make it possible to calculate all-to-all propagators with reasonable numerical costs in the HAL QCD method. We thus apply the method of HAL QCD potentials in laboratory frames to one of the simplest two hadron systems, the $I = 2$ S-wave $\pi\pi$ system at $m_\pi \approx 700$ MeV, in order to see how the theoretical formulation works in actual lattice QCD simulations. Since the $I = 2$ S-wave $\pi\pi$ system does not have quark annihilation diagrams, its interaction has been studied extensively and has been known to be repulsive at low energy [10,13,18–25]. Employing a time-dependent method reformulated for correlation functions in laboratory frames, we extract effective leading order (LO) potentials successfully from correlation functions with total momenta $|\mathbf{P}| = 2\pi/L$ and $4\pi/L$ for the first time. We then calculate physical observables such as scattering phase shifts using potentials obtained in laboratory frames, which are compared with results obtained not only from the conventional HAL QCD potential in the center of mass frame but also by the finite volume method through finite volume spectra. We confirm a consistency among all results, which validates our new method to extract HAL QCD potentials with nonzero total momenta both theoretically and numerically.

This paper is organized as follows. In Sec. II, we formulate a procedure to extract HAL QCD potentials from correlation functions in laboratory frames, using a transformation property of NBS wave functions under Lorentz transformation. In Sec. III, we present numerical results on potentials and scattering phase shifts in the $I = 2$ $\pi\pi$ system. We give summary and discussion in Sec. IV. A detailed analysis on systematic errors associated with laboratory frame calculations is given in the Appendix. Preliminary results in this study have been already reported in the conference proceedings [26].

II. HAL QCD POTENTIAL FROM THE NBS WAVE FUNCTION IN THE LABORATORY FRAME

A. Lorentz transformation of the NBS wave function

Let us consider two scalar particles with same mass m in Minkowski spacetime. The corresponding NBS wave function in a general frame of reference is defined as

$$\psi_{k_1,k_2}(x_1, x_2) = \langle 0|\mathrm{T}\{\phi(x_1)\phi(x_2)\}|k_1, k_2\rangle, \quad (1)$$

where $\phi(x)$ is a scalar field operator and $|k_1, k_2\rangle$ is an asymptotic in–state of two particles with four-momenta k_1 and k_2. Explicitly, $k_i = (\sqrt{\mathbf{k_i}^2 + m^2}, \mathbf{k}_i)$ for $i = 1, 2$. Lorentz transformation acts on field operators and asymptotic states as

$$U(\Lambda)\phi(x)U^{-1}(\Lambda) = \phi(x'), \quad (2)$$

$$U(\Lambda)|k_1, k_2\rangle = |k_1', k_2'\rangle, \quad (3)$$

where $U(\Lambda)$ is a unitary operator which implements Lorentz transformation on the states and prime symbols represent transformed objects, for example, $x'^\mu = \Lambda^\mu{}_\nu x^\nu$. Using Eqs. (1)–(3), we can derive a relation between two NBS wave functions in different frames as

$$\psi_{k_1,k_2}(x_1, x_2) = \psi_{k_1',k_2'}(x_1', x_2'). \quad (4)$$

Furthermore, a relation $\phi(x) = e^{i\hat{P}\cdot x}\phi(0)e^{-iP\cdot x}$, where $\hat{P}$ is an energy-momentum operator and $\hat{P} \cdot x = \eta_{\mu\nu}\hat{P}^\mu x^\nu$, implies that the NBS wave function is factorized into a center-of-mass plane wave and a relative wave function, $\varphi_{k_1,k_2}(x)$, as

$$\psi_{k_1,k_2}(x_1, x_2) = \varphi_{k_1,k_2}(x)e^{-iWX^0 + i\mathbf{P}\cdot\mathbf{X}}, \quad (5)$$

where $W = \sqrt{\mathbf{k}_1^2 + m^2} + \sqrt{\mathbf{k}_2^2 + m^2}$ and $\mathbf{P} = \mathbf{k}_1 + \mathbf{k}_2$ are total energy and total momentum, respectively. A center-of-mass coordinate X and a relative coordinate x are defined by

$$X = \frac{x_1 + x_2}{2}, \qquad x = x_1 - x_2. \quad (6)$$

Since $\eta_{\mu\nu}P^\mu X^\nu = WX^0 - \mathbf{P} \cdot \mathbf{X}$ is Lorentz invariant, Eqs. (4) and (5) give a relation between relative wave functions in different frames as

$$\varphi_{k_1,k_2}(x) = \varphi_{k_1',k_2'}(x'). \quad (7)$$

The HAL QCD potential is defined in the center of mass (CM) frame, whose total energy and momentum satisfy

$$W^* = \gamma(W - \mathbf{v}\mathbf{P}), \qquad \mathbf{P}^* = \gamma(\mathbf{P} - \mathbf{v}W) = 0, \quad (8)$$

where quantities with and without $*$ refer to those in the CM and laboratory (lab) frames, respectively, and a boost factor γ is defined by $\gamma = \frac{1}{\sqrt{1-\mathbf{v}^2}}$. The CM condition $\mathbf{P}^* = 0$ implies

$$\mathbf{v} = \mathbf{P}/W, \quad (W^*)^2 = W^2 - \mathbf{P}^2, \quad \gamma = \frac{W}{W^*}. \quad (9)$$

With these $\mathbf{v}$ and γ, relative coordinates in CM and lab frames are related as

$$x^{*0} = \gamma(x^0 - \mathbf{v} \cdot \mathbf{x}_\parallel), \quad \mathbf{x}^*_\parallel = \gamma(\mathbf{x}_\parallel - \mathbf{v}x^0), \quad \mathbf{x}^*_\perp = \mathbf{x}_\perp, \quad (10)$$

where $\parallel$ and $\perp$ mean vectors parallel and perpendicular to $\mathbf{v}$, respectively.

B. HAL QCD potential from the NBS wave function in the laboratory frame

We now move on to Euclidean spacetime, in which actual lattice simulations are carried out. In Euclidean coordinates, Eq. (10) reads

$$x^{*4} = \gamma(x^4 - i\mathbf{v} \cdot \mathbf{x}_\parallel), \quad \mathbf{x}^*_\parallel = \gamma(\mathbf{x}_\parallel + i\mathbf{v}x^4), \quad \mathbf{x}^*_\perp = \mathbf{x}_\perp. \quad (11)$$

In the CM frame, the relative NBS wave function at fixed x_4^* satisfies the Helmholtz equation at large separation as

$$(\nabla^{*2} + k^{*2})\varphi_{k_1^*,k_2^*}(\mathbf{x}^*, x^{*4}) = 0 (r^* = |\mathbf{x}^*| > R), \quad (12)$$

where R is an interaction range and $k^* = |\mathbf{k}^*|$ for a relative momentum $\mathbf{k}^* = \mathbf{k}_1^* = -\mathbf{k}_2^*$ in the CM frame, and its radial part with an angular momentum l behaves as [5,27]

$$\varphi^l_{k_1^*,k_2^*}(r^*, x^{*4}) \approx A_l(x^{*4}, k^*) e^{i\delta_l(k^*)} \frac{\sin(k^*r^* - l\pi/2 + \delta_l(k^*))}{k^*r^*}, \quad (13)$$

where $A_l(x^{*4}, k^*)$ is an overall factor and δ_l is the scattering phase shift, which is equal to the phase of S matrix in the scalar field theory. We construct an energy-independent nonlocal potential through the Schrödinger-type equation as

$$\frac{1}{2\mu}(\nabla^{*2} + k^{*2})\varphi_{k_1^*,k_2^*}(\mathbf{x}^*, x^{*4})$$
$$= \int d^3\mathbf{y}^* U_{x^{*4}}(\mathbf{x}^*, \mathbf{y}^*)\varphi_{k_1^*,k_2^*}(\mathbf{y}^*, x^{*4}), \quad (14)$$

where $\mu = m/2$ is the reduced mass. A subscription x^{*4} of U indicates that the potential depends on a relative time separation x^{*4} of the NBS wave function. Such a dependence is referred to as the scheme dependence of the potential [10,28]. In a general case, the potential depends on a choice of hadron operators (relative time separation,

smearing, etc.) in the NBS wave function, but physical observables extracted from potentials in different schemes, of course, agree with each other by construction.

In practice, we introduce the derivative expansion to treat the nonlocality of the potential as

$$U_{x^{*4}}(\mathbf{x}^*, \mathbf{y}^*) = \sum_i V^i_{x^{*4}}(\mathbf{x}^*)(\nabla^{*2})^i \delta(\mathbf{x}^* - \mathbf{y}^*), \quad (15)$$

where $V^i_{x^{*4}}(\mathbf{x}^*)$ are local coefficient functions in the expansion.[1] Thus, the effective leading-order (LO) potential is simply given by

$$V^{\text{LO}}_{x^{*4}}(\mathbf{x}^*) = \frac{(\nabla^{*2} + k^{*2})\varphi_{k_1^*,k_2^*}(\mathbf{x}^*, x^{*4})}{2\mu\varphi_{k_1^*,k_2^*}(\mathbf{x}^*, x^{*4})}. \quad (16)$$

Now we are ready to construct an interaction potential from the NBS wave function in the lab frame. According to Eqs. (7), (11), and (15), the relative NBS wave function in the lab frame satisfies

$$\frac{1}{2\mu}(\nabla^2_\perp + \gamma^2(\nabla_\parallel + i\mathbf{v}\partial_{x^4})^2 + k^{*2})\varphi_{k_1,k_2}(\mathbf{x}, x^4)$$
$$= \sum_i V^i_{\gamma(x^4 - i\mathbf{v}\cdot\mathbf{x}_\parallel)}(\mathbf{x}_\perp, \gamma(\mathbf{x}_\parallel + i\mathbf{v}x^4))$$
$$\times (\nabla^2_\perp + \gamma^2(\nabla_\parallel + i\mathbf{v}\partial_{x^4})^2)^i \varphi_{k_1,k_2}(\mathbf{x}, x^4). \quad (17)$$

To extract a meaningful potential from this equation, we have to set $x^4 = 0$ in order to avoid that $\mathbf{x}^*_\perp = \gamma(\mathbf{x}_\perp + i\mathbf{v}x^4)$ becomes complex. We also need to fix $\mathbf{x}_\parallel$ in order to specify x^{*4}, the scheme of the potential, since x^{*4} depends on $\mathbf{x}_\parallel$. In this paper, choosing $\mathbf{x}_\parallel = 0$, we extract a potential in the equal-time scheme. As a result, the LO potential in the equal-time scheme is given by

$$V^{\text{LO}}_{x^{*4}=0}(\mathbf{x}^*_\perp)$$
$$= \frac{(\nabla^2_\perp + \gamma^2(\nabla_\parallel + i\mathbf{v}\partial_{x^4})^2 + k^{*2})\varphi_{k_1,k_2}(\mathbf{x}, x^4)}{2\mu\varphi_{k_1,k_2}(\mathbf{x}, x^4)}\Bigg|_{x^4=0,\mathbf{x}_\parallel=0}, \quad (18)$$

where we set $x^4 = 0$ and $\mathbf{x}_\parallel = 0$ after taking derivatives in the right-hand side.

In lattice simulations, we put a system in a box of size $L \times L \times L$ with periodic boundary conditions in the lab frame. We define a correlation function of the target two-hadron system as

$$F_{\phi\phi,\mathbf{P}}(x_1, x_2) = \langle T\phi(x_1)\phi(x_2)\mathcal{J}_{\phi\phi}(\mathbf{P}, 0)\rangle, \quad (19)$$

---

[1]We do not include terms with odd powers of ∇ here. This choice can be also regarded as a scheme of the potential.

where $\mathcal{J}_{\phi\phi}(\mathbf{P}, 0)$ creates two-particle states with total momentum $\mathbf{P}$ at $X^4 = 0$, which is quantized as $\mathbf{P} = \frac{2\pi}{L}\mathbf{n}_{\text{total}}(\mathbf{n}_{\text{total}} \in \mathbf{Z}^3)$. This correlation function can be written as

$$F_{\phi\phi,\mathbf{P}}(x_1, x_2) = e^{i\mathbf{P}\cdot\mathbf{X}}\sum_{\mathbf{n}}B_{\mathbf{n}}\varphi_{W_{\mathbf{n}}}(x)e^{-W_{\mathbf{n}}X^4}$$

$$+ (\text{inelastic contributions}) \qquad (20)$$

$$\rightarrow e^{i\mathbf{P}\cdot\mathbf{X}}B_{\min}\varphi_{W_{\min}}(x)e^{-W_{\min}X^4}, \quad (X^4 \gg 1), \quad (21)$$

where

$$W_{\mathbf{n}} = \sqrt{\mathbf{k}_1 + m^2} + \sqrt{\mathbf{k}_2 + m^2}, \quad \mathbf{k}_1 + \mathbf{k}_2 = \mathbf{P}, \qquad (22)$$

$$B_{\mathbf{n}} = \langle k_1, k_2|\mathcal{J}_{\phi\phi}(\mathbf{P}, 0)|0\rangle,$$

$$k_1^0 = \sqrt{\mathbf{k}_1 + m^2}, \qquad k_2^0 = \sqrt{\mathbf{k}_2 + m^2}. \qquad (23)$$

$W_{\min}$ is the minimum value among $W_{\mathbf{n}}$, and corresponding $B_{\mathbf{n}}$ and $\varphi_{\mathbf{n}}$ denote $B_{\min}$ and $\varphi_{\min}$, respectively. Therefore, we can extract the NBS wave function of the lowest energy state through this correlation function at a large CM time X^4. Note that these relative NBS wave functions have a periodicity depending on $\mathbf{P} = \frac{2\pi}{L}\mathbf{n}_{\text{total}}$ as

$$\varphi_W(\mathbf{x} + \mathbf{m}L, x^4)e^{i\pi\mathbf{n}_{\text{total}}\cdot\mathbf{m}} = \varphi_W(\mathbf{x}, x^4) \quad (\mathbf{n}_{\text{total}}, \mathbf{m} \in \mathbf{Z}^3), \qquad (24)$$

which can be derived from Eq. (5), together with the periodicity of coordinates $\mathbf{x_i}$ ($i = 1, 2$). Calculations of derivatives (e.g., $\nabla_\parallel$ at $\mathbf{x}_\parallel = 0$) are implemented by taking this periodicity into account. In summary, we can extract the effective LO potential from $F_{\phi\phi}(x_1, x_2)$ at sufficiently large X^4 through Eq. (18) in lattice simulations.

C. Time-dependent method in the laboratory frame

Since correlation functions generally become noisier at larger X^4 in lattice QCD simulations, it is difficult to achieve Eq. (21) within good precision. To overcome this difficulty, we have introduced the time-dependent method for an extraction of potentials in the CM frame [7], which does not require a single state dominance in $F_{\phi\phi}$ such as Eq. (21). This method enables us to extract interaction potentials at smaller X^4 with less statistical fluctuations. We here discuss how we extend the time dependent method to the lab frame.

A key quantity in the time-dependent method is a normalized correlation function R (we call it "R correlator"), which is defined in the lab frame as

$$R(\mathbf{x}, x^4, X^4) = \frac{F_{\phi\phi,\mathbf{P}}(\mathbf{x}, x^4, X^4)}{F_{\phi,1}(X^4)F_{\phi,2}(X^4)}, \qquad (25)$$

where

$$F_{\phi\phi,\mathbf{P}}(\mathbf{x}, x^4, X^4)$$
$$= \sum_{\mathbf{X}}e^{-i\mathbf{P}\cdot\mathbf{X}}\langle \mathrm{T}\phi(X + x/2)\phi(X - x/2)\mathcal{J}_{\phi\phi}(\mathbf{P}, 0)\rangle, \qquad (26)$$

$$F_{\phi,i}(X^4) = \sum_{\mathbf{x},\mathbf{y}}e^{i\mathbf{p}_i\cdot(\mathbf{y}-\mathbf{x})}\langle \phi(\mathbf{x}, X^4)\phi^\dagger(\mathbf{y}, 0)\rangle. \qquad (27)$$

A summation over the CM coordinate $\mathbf{X}$ with a factor $e^{-i\mathbf{P}\cdot\mathbf{X}}$ in Eq. (26) removes the unnecessary plane wave factor $e^{i\mathbf{P}\cdot\mathbf{X}}$ in Eq. (19) and reduces statistical fluctuations. In general, a normalization of the R correlator, namely the choice of two-point functions in the denominator in Eq. (25), is not unique. One natural choice is a normalization using the lowest energy in a noninteracting system. For example, if a source operator is given by $\bar{\mathcal{J}}_{\phi\phi}(\mathbf{P}, 0) = \sum_{\mathbf{x},\mathbf{y}}e^{i\mathbf{p}_1\cdot\mathbf{x}}e^{i\mathbf{p}_2\cdot\mathbf{y}}\bar{\phi}(\mathbf{x}, 0)\bar{\phi}(\mathbf{y}, 0)$ with $\mathbf{P} = \mathbf{p}_1 + \mathbf{p}_2$, we then take $F_{\phi,1}(T) = \sum_{\mathbf{x},\mathbf{y}}e^{i\mathbf{p}_1\cdot(\mathbf{y}-\mathbf{x})}\langle \phi(\mathbf{x}, T)\bar{\phi}(\mathbf{y}, 0)\rangle$ and $F_{\phi,2}(T) = \sum_{\mathbf{x},\mathbf{y}}e^{i\mathbf{p}_2\cdot(\mathbf{y}-\mathbf{x})}\langle \phi(\mathbf{x}, T)\bar{\phi}(\mathbf{y}, 0)\rangle$ in Eq. (25). Alternatively, we may choose hadron masses measured in the center-of-mass frame for the normalization. While such a difference in normalizations does not affect final results of potentials in the continuum limit, it may produce some systematic uncertainties in potentials due to discretization errors at finite lattice spacings. Since meson energies in the laboratory frame suffer from larger discretization effects due to nonzero momenta, it is important to keep such effects under control in our numerical simulation, which will be investigated in the Appendix. In the rest of our paper, we employ the normalization using the lowest energy in the noninteracting system.

At a moderately large X^4 where inelastic contributions can be neglected, $R(\mathbf{x}, x^4, X^4)$ behaves as

$$R(\mathbf{x}, x^4, X^4) \approx \sum_{\mathbf{n}}B'_{\mathbf{n}}\varphi_{W_{\mathbf{n}}}(\mathbf{x}, x^4)e^{-W_{\mathbf{n}}X^4}, \qquad (28)$$

where $B'_{\mathbf{n}} = \frac{B_{\mathbf{n}}}{C_1 C_2}$, and

$$F_{\phi,i}(X^4) = C_i e^{-\sqrt{m^2+p_i^2}X^4} + (\text{inelastic contributions}). \qquad (29)$$

By considering Eqs. (17) and (28), we can show that

$$\frac{1}{m}[\nabla_\perp^2 G(\mathbf{x}, x^4, X^4) + (-(\partial_{X^4} - W_{0,\text{free}})\nabla_\parallel + i\mathbf{P}\partial_{x^4})^2 R(\mathbf{x}, x^4, X^4)]$$

$$+ \frac{1}{4m}[\partial_{X^4}^2 - 2W_{0,\text{free}}\partial_{X^4} + W_{0,\text{free}}^2 - \mathbf{P}^2 - 4m^2]G(\mathbf{x}, x^4, X^4)\Big|_{x^4=0, \mathbf{x}_\parallel=0}$$

$$\approx \sum_\mathbf{n} B'_\mathbf{n} W_{\text{CM},\mathbf{n}}^2 \frac{1}{m}[\nabla_\perp^2 + \gamma_\mathbf{n}^2(\nabla_\parallel + i\mathbf{v_n}\partial_{x^4})^2 + k_\mathbf{n}^{*2}]\varphi_{W_\mathbf{n}}(\mathbf{x}, x^4)e^{-(W_\mathbf{n} - W_{0,\text{free}})X^4}\Big|_{x^4=0, \mathbf{x}_\parallel=0}$$

$$= \sum_j V_{x^{*4}=0}^j(\mathbf{x}_\perp^*) \sum_\mathbf{n} B'_\mathbf{n} W_{\text{CM},\mathbf{n}}^2 (\nabla_\perp^2 + \gamma_\mathbf{n}^2(\nabla_\parallel + i\mathbf{v_n}\partial_{x^4})^2)^j \varphi_{W_\mathbf{n}}(\mathbf{x}, x^4)e^{-(W_\mathbf{n} - W_{0,\text{free}})X^4}\Big|_{x^4=0, \mathbf{x}_\parallel=0}$$

$$\approx \sum_j V_{x^{*4}=0}^j(\mathbf{x}_\perp^*)((\nabla^{*2})^j G(x, x^4, X^4)),\Big|_{x^4=0, \mathbf{x}_\parallel=0}, \tag{30}$$

where $W_{0,\text{free}} = \sqrt{m^2 + p_1^2} + \sqrt{m^2 + p_2^2}$ is a noninteracting energy level used in the normalization and $\gamma_\mathbf{n}^2 = \frac{W_\mathbf{n}^2}{W_{\text{CM},\mathbf{n}}^2}$, and we introduce a short-hand notation $G(\mathbf{x}, x^4, X^4)$ as

$$G(\mathbf{x}, x^4, X^4) = ((\partial_{X^4} - W_{0,\text{free}})^2 - \mathbf{P}^2)R(\mathbf{x}, x^4, X^4). \tag{31}$$

Note that we can move V^j outside a summation over $\mathbf{n}$ for elastic states in Eq. (30) only at $x^{*4} = 0$, since a scheme of the potential depends on $\mathbf{n}$ through $\gamma_\mathbf{n}$ unless $x^{*4} = \gamma_\mathbf{n}(x^4 - i\mathbf{v_n} \cdot \mathbf{x}_\parallel) = 0$. The effective LO potential in the time-dependent method is given by

$$V_{x^{*4}=0}^{\text{LO}}(\mathbf{x}_\perp) = \frac{(L_\perp + L_\parallel + mE)(\mathbf{x}, x^4, X^4)}{mG(\mathbf{x}, x^4, X^4)}\Big|_{x^4=0, \mathbf{x}_\parallel=0}, \tag{32}$$

where we introduce new notations $L_\perp, L_\parallel$ for the Laplacian part and E for the energy part as

$$L_\perp(\mathbf{x}, x^4, X^4) = \nabla_\perp^2 G(\mathbf{x}, x^4, X^4), \tag{33}$$

$$L_\parallel(\mathbf{x}, x^4, X^4) = (-(\partial_{X^4} - W_{0,\text{free}})\nabla_\parallel + i\mathbf{P}\partial_{x^4})^2 R(\mathbf{x}, x^4, X^4), \tag{34}$$

$$E(\mathbf{x}, x^4, X^4) = \frac{1}{4m}[\partial_{X^4}^2 - 2W_{0,\text{free}}\partial_{X^4} + W_{0,\text{free}}^2$$
$$- \mathbf{P}^2 - 4m^2]G(\mathbf{x}, x^4, X^4), \tag{35}$$

for later convenience. This procedure is more complicated than the conventional time-dependent method [7], since we need to sum over $\mathbf{n}$ without knowing not only $k_\mathbf{n}^{*2}$ but also Lorentz factor $\gamma_\mathbf{n}^2$ and velocity $\mathbf{v_n}$ for each $\mathbf{n}$, by combining several terms as shown above.

III. NUMERICAL RESULTS IN THE $I = 2$ $\pi\pi$ SYSTEM

A. Calculation of correlation functions

Let us consider the $I = 2$ $\pi\pi$ S-wave scattering as an explicit example. We define correlation functions of this system as

$$F_{\pi^+\pi^+,\mathbf{P}}(\mathbf{x}, x^4, X^4)$$
$$= \sum_\mathbf{X} e^{-i\mathbf{P}\cdot\mathbf{X}}\langle T\pi^+(X + x/2)\pi^+(X - x/2)\mathcal{J}_{\pi^+\pi^+}(\mathbf{P}, 0)\rangle, \tag{36}$$

$$F_{\pi^+,i}(X^4) = \sum_{\mathbf{x},\mathbf{y}} e^{i\mathbf{p}_i\cdot(\mathbf{y}-\mathbf{x})}\langle\pi^+(\mathbf{x}, X_4)\pi^-(\mathbf{y}, 0)\rangle, \tag{37}$$

where the positively (negatively) charged pion operator is constructed in terms of up and down quark fields $u(x)$ and $d(x)$ as $\pi^+(x) = \bar{d}(x)\gamma_5 u(x)$ $[\pi^-(x) = \bar{u}(x)\gamma_5 d(x)]$. Total momenta are chosen as $\mathbf{P} = (P_x, P_y, P_z) = \frac{2\pi}{L}(0, 0, n)$ $(n = 0, 1, 2)$, and corresponding source operators are given by

$$\mathcal{J}_{\pi^+\pi^+}(\mathbf{P} = (0, 0, 0), 0) = \bar{\pi}_s^+(\mathbf{p_1} = \mathbf{0}, 0)\bar{\pi}_s^+(\mathbf{p_2} = \mathbf{0}, 0), \tag{38}$$

$$\mathcal{J}_{\pi^+\pi^+}(\mathbf{P} = (0, 0, 1), 0)$$
$$= \bar{\pi}_s^+(\mathbf{p_1} = (0, 0, 1), 0)\bar{\pi}_s^+(\mathbf{p_2} = \mathbf{0}, 0), \tag{39}$$

$$\mathcal{J}_{\pi^+\pi^+}(\mathbf{P} = (0, 0, 2), 0)$$
$$= \bar{\pi}_s^+(\mathbf{p_1} = (0, 0, 1), 0)\bar{\pi}_s^+(\mathbf{p_2} = (0, 0, 1), 0), \tag{40}$$

where all momenta are given in unit of $2\pi/L$, and we keep this notation in the remaining of this paper. A pion creation operator with momentum is defined as

$$\bar{\pi}^+(\mathbf{p}, 0) = \sum_\mathbf{y} \pi^-(\mathbf{y}, 0)e^{+i\mathbf{p}\cdot\mathbf{y}}, \tag{41}$$

and a subscript s indicates that quark fields in operators are smeared to suppress inelastic contributions at earlier imaginary time, as will be explained in Sec. III B. As already mentioned, we also consider another normalization of the R correlator to study systematic uncertainty. We find that this systematic uncertainty affects the potential fitting and scattering phase shift (for example, see Fig. 16). Detailed analysis can be found in the Appendix.

For calculations of correlation functions defined above, we employ the one-end trick [29], which enables us to evaluate a combination of two all-to-all propagators with spatial summation by a single stochastic estimator.

B. Simulation details

We employ $2 + 1$ flavor full QCD configurations generated by CP-PACS Collaborations [30] on a $32^3 \times 64$ lattice with the Iwasaki gauge action [31] at $\beta = 1.90$ and the nonperturbatively improved Wilson-clover action [32] at $c_{\mathrm{SW}} = 1.7150$, which corresponds to the lattice spacing $a = 0.0907$ fm. Hopping parameters $(\kappa_{ud}, \kappa_s) = (0.13700, 0.13640)$ lead to the pion mass $m_\pi \approx 700$ MeV. A periodic boundary condition is employed in all spacetime directions. Correlation functions with $\mathbf{P} \neq 0$ ($\mathbf{P} = 0$) are evaluated by 399 gauge configurations × 64 time slices (399 gauge configurations × 16 time slices), and we estimate statistical errors by the jackknife method with a bin-size 21 in all cases. We label results with $P = (0, 0, n)$ ($n = 0, 1, 2$) as CM, case 1, and case 2, respectively. Hereafter dimensionful quantities without corresponding unit are written in lattice unit unless otherwise stated.

We employ the smeared quark source $q_s(\mathbf{x}, t) = \sum_{\mathbf{y}} f(\mathbf{x} - \mathbf{y}) q(\mathbf{y}, t)$ with the Coulomb gauge fixing, where the smearing function $f(\mathbf{x})$ is taken as [33]

$$f(\mathbf{x}) = \begin{cases} A e^{-B|\mathbf{x}|} & (0 < |\mathbf{x}| < (L-1)/2) \\ 1 & (|\mathbf{x}| = 0) \\ 0 & (|\mathbf{x}| \geq (L-1)/2) \end{cases}, \quad (42)$$
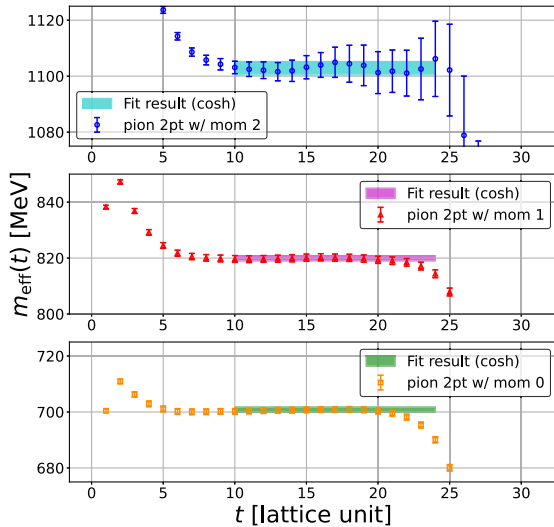
with $A = 1.2$, $B = 0.30$. We generate a single Z_4 noise vector for each insertion of the one-end trick. To reduce stochastic noise contaminations from noise vectors, the dilution technique [34] is applied to color, spinor, and spatial indices. We fully dilute color and spinor indices, and $s2$ (even-odd) dilution [12] is taken for the spatial index. Numerical derivatives are approximated by second order differences. In estimations of x^4 derivatives, we utilize correlation functions with even relative time $x^4 = 0, \pm 2$ to keep the CM time X^4 integer.

Since our formulation relies on the continuum dispersion relation, we first check a behavior of a pion dispersion relation. Figure 1 (left) shows effective energies of a single pion with momenta $\mathbf{p} = (0, 0, n)$ ($n = 0, 1, 2$). We obtain good plateaus for all cases thanks to the quark smearing. An energy eigenvalue for each momentum channel is extracted by a single cosh fit, as shown by light color bands in Fig. 1 (left). We then compare those to the continuum dispersion relation, $E(p) = \sqrt{m_\pi^2 + \mathbf{p}^2}$. As seen in Fig. 1 (right), extracted energy levels (blue points) are consistent with the continuum dispersion relation (black solid line) up to $|p| = 4\pi/L$, so that we can safely utilize the continuum dispersion relation in this study.

C. The NBS wave function in the laboratory frame

Before discussing the interaction potential, let us consider the behavior of $F_{\pi^+\pi^+, \mathbf{P}}$ defined in Eq. (36). As already discussed in Eqs. (20) and (21), we can extract ground state energies and corresponding NBS wave functions at $X^4 \gg 1$. Figure 2 (left) shows effective energies obtained from the X^4 dependence of $\sum_{\mathbf{x}} F_{\pi^+\pi^+, \mathbf{P}}(\mathbf{x}, x^4 = 0, X^4)$ and
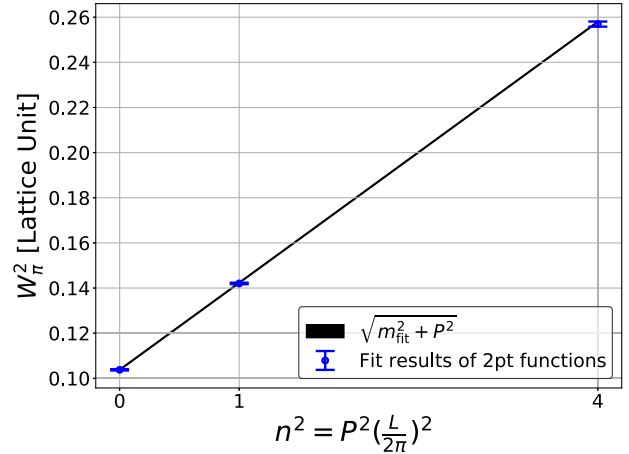
FIG. 1.   Left: effective energies of a single pion with $|p| = 0$ (orange square), $|p| = 2\pi/L$ (red triangle), and $|p| = 4\pi/L$ (blue circle). Fit results using a cosh function and corresponding fit ranges are shown by light color bands. Right: a comparison between extracted energy levels (blue points) and the continuum dispersion relation, $E(p) = \sqrt{m_{\pi,\mathrm{fit}}^2 + p^2}$ (black solid line). For $m_{\pi,\mathrm{fit}}$, we use the fit result of 2pt correlation function with $|p| = 0$ (green band in the bottom of the left figure).
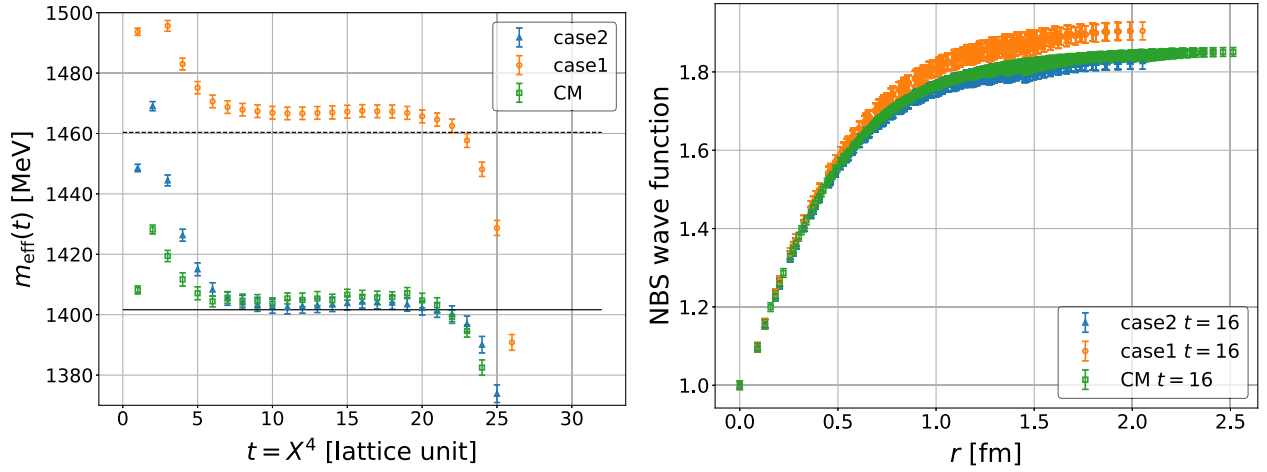
FIG. 2. Left: effective energies obtained by spatial summation of $F_{\pi^+\pi^+,\mathbf{P}}$. Laboratory frame energies are boosted back to the CM frame via $W_{\mathrm{CM}}^2 = W_{\mathrm{L}}^2 - P^2$. Dashed and solid lines show the lowest noninteracting energies with $\mathbf{P} = (0,0,2\pi/L)$ and $(0,0,4\pi/L)$, respectively. Right: spatial dependence of $F_{\pi^+\pi^+,\mathbf{P}}$. For $|P| \neq 0$, we fix $\mathbf{x}_\parallel = \mathbf{0}$ and only show $\mathbf{x}_\perp$ dependence. Values at the origin are normalized to unity.

corresponding noninteracting energy levels (horizontal lines). We observe that all effective energies reach plateaus at around $X^4 = 15$, and they slightly shift upward from the noninteracting energy levels. It indicates that $F_{\pi^+\pi^+,\mathbf{P}}$ is almost dominated by the ground state at that time slice and the interaction is repulsive as reported in previous studies [10,13,24]. In the Fig. 2 (right), we show the spatial dependence of the $F_{\pi^+\pi^+,\mathbf{P}}(\mathbf{x}_\perp, \mathbf{x}_\parallel = 0, x^4 = 0, X^4)$ at $t = X^4 = 16$, which is expected to approach the ground state NBS wave function in the CM frame in accordance with Eq. (21) as

$$F_{\pi^+\pi^+,\mathbf{P}}(\mathbf{x}_\perp, \mathbf{x}_\parallel = 0, x^4 = 0, X^4)$$
$$\approx B_{\min}\varphi_{W_{\min}}(\mathbf{x}_\perp, \mathbf{x}_\parallel = 0, x^4 = 0)e^{-W_{\min}X^4}$$
$$= B_{\min}\varphi_{W_{\min}^*}(\mathbf{x}_\perp^* = \mathbf{x}_\perp, \mathbf{x}_\parallel^* = 0, x^{*4} = 0)e^{-W_{\min}X^4}. \quad (43)$$

A small number of data points in $|P| \neq 0$ is due to the condition of the equal-time scheme, $(\mathbf{x}_\parallel, x^4) = (\mathbf{0}, 0)$. As expected by the behavior of effective energies, they show the monotonic increasing behaviors in r, typical for the repulsive force. Moreover, the NBS wave function with $|P| = 4\pi/L$ (case 2) is very similar to that with $|P| = 0$ (CM), probably due to a fact that the lowest energy with $|P| = 4\pi/L$ boosted back to the CM frame is roughly equal to the one with $|P| = 0$, as seen in Fig. 2 (left).

D. Effective leading-order potential

We next consider effective leading order (LO) potentials obtained by the time-dependent method. Figure 3 shows effective LO potentials with three different total momenta at $t = X^4 = 16$. As already discussed in Sec. III C, potentials show repulsive behaviors, and they are consistent with each other except at short distances. A small difference

observed at short distances may be explained by finite lattice spacing effects.

We also observe that potentials in cases 1 and 2 have larger statistical errors and nonsmooth behaviors as compared with that in the CM case. Typically, introducing nonzero momentum makes correlation functions noisier, since an enhancement of statics by the translational invariance is reduced. Indeed, we have already observed that NBS wave functions themselves are noisier than the one in the CM frame [see Fig. 2 (right)]. In addition, larger statistical fluctuations in the laboratory frame are probably caused also by fourth-order X^4 derivative terms in the time-dependent method. To estimate fourth-order X^4 derivatives at a fixed X^4 by the numerical difference, we have to utilize correlation functions at $X^4 \pm 2$, which are absent for second-order derivatives. Since data at larger X^4 are
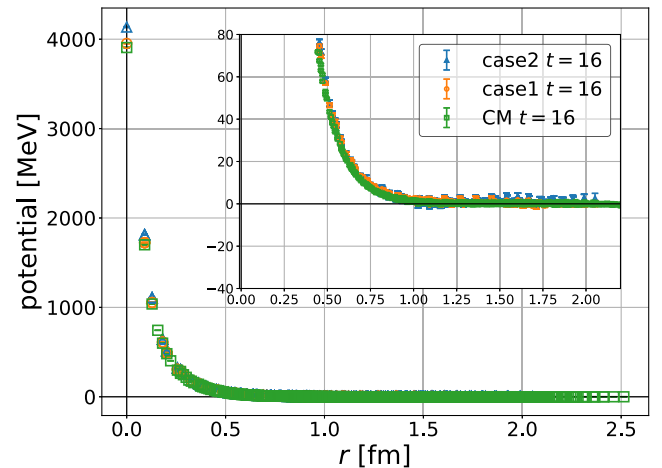
FIG. 3. A comparison of all effective LO potentials. Inset shows an enlarged view of the potentials.
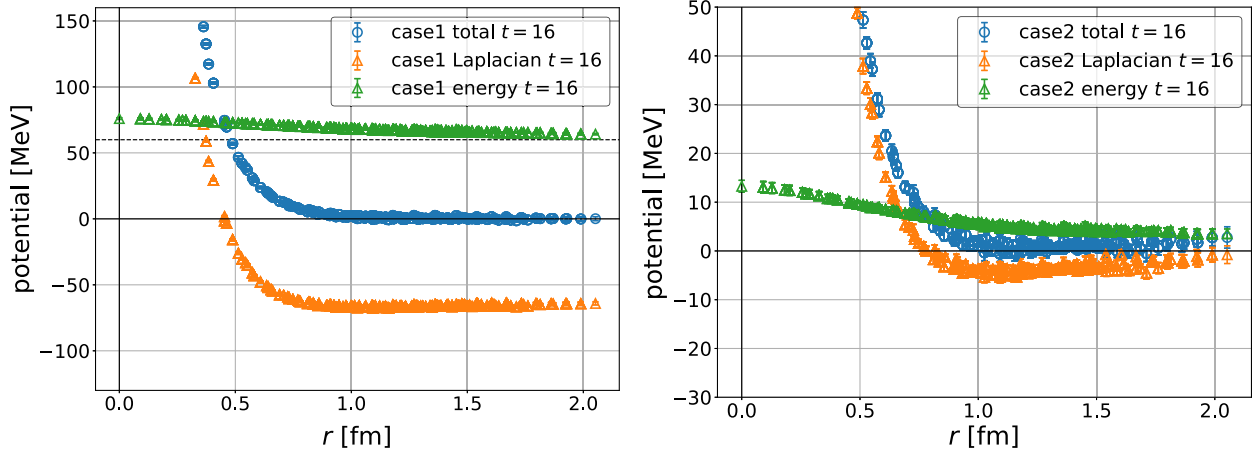
FIG. 4. A decomposition of the effective LO potential in case 1 (left) and case 2 (right). A dotted line represents an expected relative energy in a noninteracting case.

generally nosier, fourth-order X^4 derivatives are expected to be noisier as well. Nonsmooth behaviors for potentials in the laboratory frame, on the other hand, may be explained by a contamination from the $l = 2$ partial wave, which is absent in the CM frame, as follows. In the laboratory frame calculation, the cubic rotation is no longer the symmetry

of the system, since the cubic box is deformed by the Lorentz contraction if it is boosted back to the CM frame. In our setup, since the box becomes a rectangular with size $L \times L \times \gamma L$ with a boost factor γ in the CM frame, the cubic symmetry is reduced to the one which makes this rectangular intact. An irreducible representation A_1^+ of the reduced
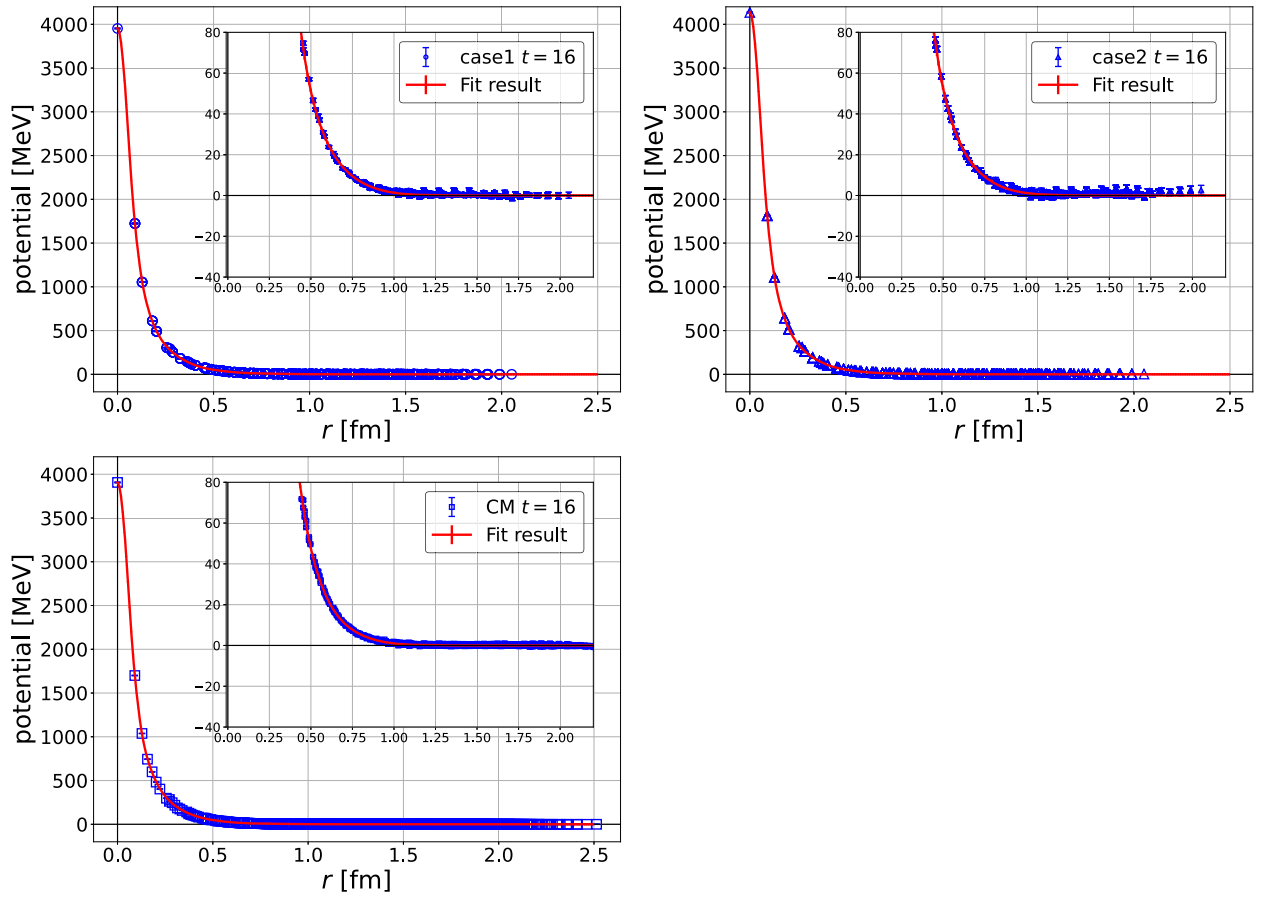
FIG. 5. Fit results of effective LO potentials. Original data (blue points) and corresponding fit results (red lines) are shown.

TABLE I.   Fit parameters of potentials at $t = X^4 = 16$.

	a_0	a_1	a_2	a_3	a_4	a_5	a_6	a_7	χ^2/d.o.f.
Case 1	0.5579(72)	1.410(32)	0.2551(58)	2.86(10)	0.052(11)	5.24(24)	0.953(22)	0.7719(62)	7.28
Case 2	0.5711(95)	1.433(51)	0.2618(75)	2.88(16)	0.055(19)	5.15(44)	1.014(34)	0.7809(87)	2.30
CM	0.474(10)	1.589(75)	0.206(12)	3.04(19)	0.045(15)	5.16(34)	1.070(36)	0.813(11)	2.57

symmetry contains contributions from angular momenta $l = 0, 2, \ldots$, in contrast to the A_1^+ in the cubic symmetry, which allows $l = 0, 4, 6, \ldots$ partial waves. Since lower partial waves in general have larger contributions at low energy, a contamination form the $l = 2$ partial wave causes nonsmooth behaviors of potentials in the laboratory frame, which is stronger than the one by the $l = 4$ partial wave, the lowest partial wave contamination in the CM frame.

To see how the time-dependent method works in detail, we decompose potentials into the Laplacian term, $\frac{L_\perp + L_\parallel}{mG}$ in Eq. (32), and the energy term, $\frac{mE}{mG}$ in Eq. (32), as shown in Fig. 4. We observe that the Laplacian term (orange) and the energy term (green) are away from zero, but the total (blue) converges to zero at large distances thanks to their cancellations. Since values of the energy shift (green) roughly agree with expectations from lowest energies in noninteracting cases, the cancellation of two terms (orange and green) is a strong evidence on the validity of the time-dependent method with nonzero total momenta.

In conclusion, we confirm that potentials can be extracted at reasonable precision in the laboratory frame formalism of the HAL QCD method. One lesson we learn is that we need more statistics than required in the conventional center-of-mass formalism.

E. Scattering phase shifts

To investigate a consistency between calculations in the lab frame and the CM frame more precisely, let us compare behaviors of physical observables, such as scattering phase shifts $\delta_0(k)$ and $k \cot \delta_0(k)$. We fit effective LO potentials with a sum of four Gaussians,

$$V(r) = a_0 e^{-(r/a_1)^2} + a_2 e^{-(r/a_3)^2} + a_4 e^{-(r/a_5)^2} + a_6 e^{-(r/a_7)^2}, \tag{44}$$

and solve the Schrödinger equation in infinite-volume. Representative fit results and corresponding fit parameters are given in Fig. 5 and Table I, respectively. As seen from the table, values of χ^2/d.o.f. are rather large, mainly due to data at short distances, which have smaller errors but whose central values show scattered behaviors caused by higher partial waves. Since fits in Fig. 5 looks reasonable in all cases, we keep using the fitting function (44). We study systematic uncertainties of potential fits caused by discretization errors, whose details will be given in the Appendix. Error bands in the following plots include both statistical

and systematic errors. As you can see from Fig. 6, resultant scattering phase shifts obtained by the lab frame calculations (blue and orange bands) are consistent with the conventional CM calculation (red band), as expected from the agreement of potentials.

Finally, we compare our results with those obtained by the finite-volume method. We extract ground state energies by a single exponential fit to the time dependence of the R correlators, as shown in Fig. 7. Energy levels are converted to the center-of-mass relative momentum k_n, to which the Lüscher's formula is applied as

$$k_n \cot \delta_0(k_n) = 4\pi \frac{1}{\gamma_n L^3} \sum_{\mathbf{p} \in \mathcal{P}_{\mathbf{n}_{\text{total}}}} \frac{1}{\mathbf{p}^2 - k_n^2}, \tag{45}$$

where

$$\mathcal{P}_{\mathbf{n}_{\text{total}}} = \left\{ \mathbf{p} \middle| \mathbf{p} = \frac{2\pi}{L} \vec{\gamma}^{-1} \left(\mathbf{m} + \frac{1}{2} \mathbf{n}_{\text{total}} \right), \mathbf{m} \in \mathbb{Z}^3 \right\}, \tag{46}$$

with a short-hand notation $\vec{\gamma}^{-1} \mathbf{n} = \gamma^{-1} \mathbf{n}_\parallel + \mathbf{n}_\perp$. Extracted values of $k \cot \delta_0(k)$ are plotted in Fig. 8 (right), together with a result in the literature [24]. As seen in the figure, we confirm that phase shifts obtained by the HAL QCD method are consistent with those by the finite-volume method. It also implies that the LO approximation is valid in the energy region we consider here, since the
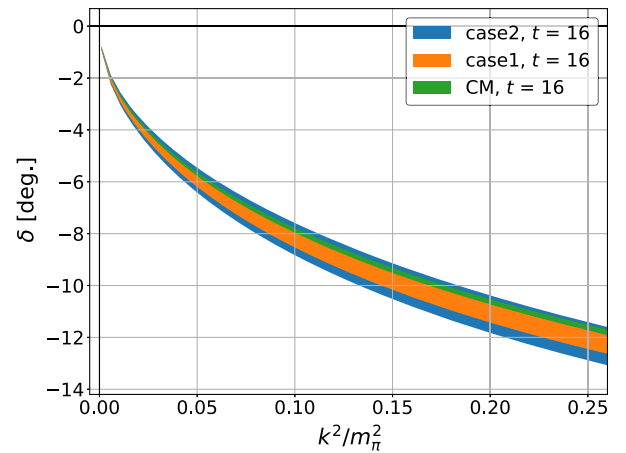
FIG. 6.   Scattering phase shifts obtained by effective LO potentials. Color bands show statistical and systematical errors added linearly. Detailed discussion of systematic errors is given in the Appendix.
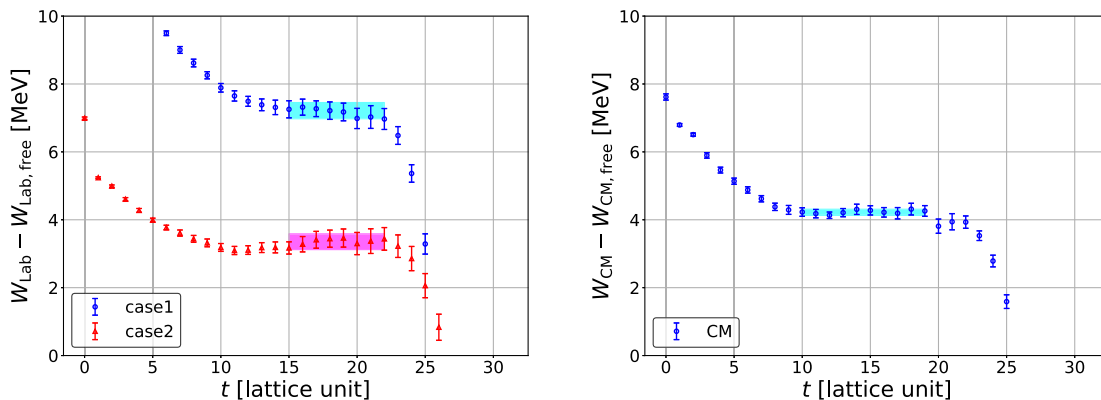
FIG. 7.   Extraction of energy shifts by single exponential fits in the laboratory frame (left) and the center-of-mass frame (right). Color bands show fit ranges and fit results with statistical errors.
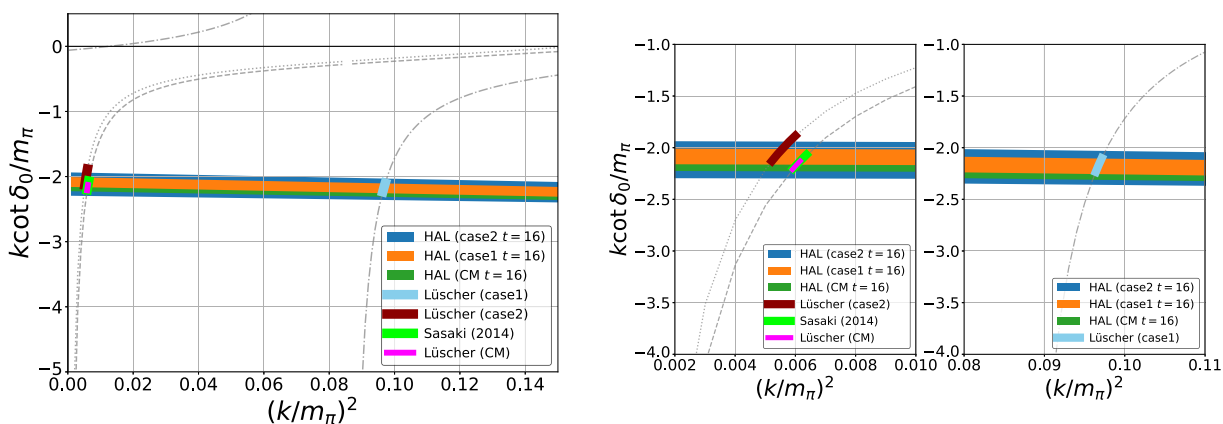
FIG. 8.   A comparison of $k \cot \delta_0(k)$ between the HAL QCD method and the Lüscher's method. Shown together are lines of the Lüscher's formula. Left: entire view. Right: enlarged view of the left figure.

finite-volume method is free from systematics associated with the derivative expansion.

IV. SUMMARY

In this paper, we propose a theoretical framework to calculate HAL QCD potentials from NBS wave functions in laboratory frames and perform a first numerical calculation in the $I = 2$ $\pi\pi$ system at $m_\pi \approx 700$ MeV. We calculate effective LO potentials from NBS wave functions with total momenta $P = (0, 0, n)$ $(n = 0, 1, 2)$. While larger statistical fluctuations and nonsmooth behaviors, which are probably originated from higher order numerical derivatives and the reduced rotational symmetry, have been observed in laboratory frames $(n = 1, 2)$, potentials in all cases $(n = 0, 1, 2)$ are repulsive and agree with each other except small deviations at short distances. Resultant phase shifts $\delta_0(k)$ and $k \cot \delta_0(k)$ with $n = 1, 2$ are consistent with those obtained not only by the conventional center-of-mass calculation $(n = 0)$ but also by the finite-volume method. In conclusion, we confirm that the laboratory

frame formalism works in practice to extract scattering phase shifts in lattice QCD. As already mentioned in Sec. I, it enlarges applicabilities and opens new possibilities for the HAL QCD method, such as determinations of higher-order terms in the derivative expansion of nonlocal potentials and extractions of potentials for systems having same quantum numbers with a vacuum state.

We finally discuss some issues for a use of laboratory frames in the HAL QCD method. As already mentioned, statistical fluctuations are larger in laboratory frames, probably due to larger energy of states with nonzero momenta and higher order time derivatives necessary for the time dependent method. While a number of statistical sampling required for meaningful results is manageably small for the $I = 2$ $\pi\pi$ system, it may drastically increase for more complicated systems including quark-antiquark pair creations and annihilations. Nonsmooth behaviors of potentials, caused by reduced symmetries in laboratory frames, may be cured by the partial wave decomposition technique [35], though the technique is restricted to the center-of-mass system at this moment. Since larger nonzero

momenta may cause lager discretization errors through violations of continuum dispersion relations, we should always check a validity of the continuum dispersion relation. In addition, it is better to compare different normalizations of R correlators for potentials, as discussed in the Appendix.

APPENDIX: SYSTEMATIC UNCERTAINTIES

In this appendix, we estimate systematic uncertainties on extractions of $I = 2$ S-wave $\pi\pi$ scattering phase shifts in laboratory frames. Concretely, we investigate a normalization dependence and an X^4 dependence of the potential extraction with nonzero total momenta.

For the former investigation, we consider an alternative time-dependent method using R-correlators normalized differently as

$$R_{\mathbf{P}=\mathbf{e_z}}(\mathbf{x}, x^4, X^4) = \frac{F_{\pi^+\pi^+,\mathbf{e_z}}(\mathbf{x}, x^4, X^4)}{F_{\pi^+,0}(X^4)^2}, \quad \text{(A1)}$$

$$R_{\mathbf{P}=2\mathbf{e_z}}(\mathbf{x}, x^4, X^4) = \frac{F_{\pi^+\pi^+,2\mathbf{e_z}}(\mathbf{x}, x^4, X^4)}{F_{\pi^+,0}(X^4)^2}, \quad \text{(A2)}$$
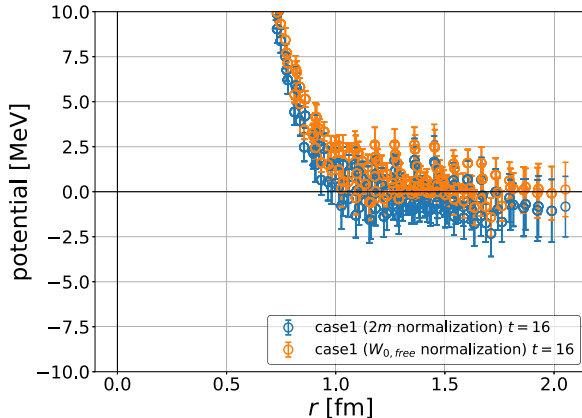
where $F_{\pi^+,0}(X^4) = \sum_{\mathbf{x},\mathbf{y}}\langle\pi^+(\mathbf{x}, X_4)\pi^-(\mathbf{y}, 0)\rangle$ is a pion 2-pt function with *zero* momentum. Building blocks of potentials are thus modified to

$$G(\mathbf{x}, x^4, X^4) = ((\partial_{X^4} - 2m)^2 - \mathbf{P}^2)R_{\mathbf{P}}(\mathbf{x}, x^4, X^4), \quad \text{(A3)}$$

$$E(\mathbf{x}, x^4, X^4) = \frac{1}{4m}[\partial_{X^4}^2 - 4m\partial_{X^4} - \mathbf{P}^2]G(\mathbf{x}, x^4, X^4), \quad \text{(A4)}$$

$$L_\perp(\mathbf{x}, x^4, X^4) = \nabla_\perp^2 G(\mathbf{x}, x^4, X^4), \quad \text{(A5)}$$

$$L_\parallel(\mathbf{x}, x^4, X^4) = (-(\partial_{X^4} - 2m)\nabla_\parallel + i\mathbf{P}\partial_{x^4})^2 R_{\mathbf{P}}(\mathbf{x}, x^4, X^4), \quad \text{(A6)}$$

which should be compared with Eqs. (31)–(34). Using these, the LO potential is constructed as

$$V_{x^{*4}=0}^{\text{LO}}(\mathbf{x}_\perp) = \frac{(L_\perp + L_\parallel + mE)(\mathbf{x}, x^4, X^4)}{mG(\mathbf{x}, x^4, X^4)}\Bigg|_{x^4=0, \mathbf{x}_\parallel=0}, \quad \text{(A7)}$$

which is expected to agree with the one in (32) within systematics errors. Therefore, we can estimate the systematics from a difference between two potentials with different normalizations.

For the latter, we simply compare potentials at $X^4 = 16 \pm 1$. In the following, we show both dependences and present an estimation of uncertainties on scattering phase shifts.

1. Normalization dependence

Figure 9 shows the normalization dependence of effective LO potentials, the $W_{0,\text{free}}$ normalization (orange) defined in Eq. (32) and the $2m$ normalization (blue) in Eq. (A7), with nonzero total momenta, $\mathbf{P} = \mathbf{e_z}$ (left) and $\mathbf{P} = 2\mathbf{e_z}$ (right). We observe a slight systematic downward shift of central values for the LO potential with the $2m$ normalization, though differences are comparable with sizes of statistical errors, and these shifts mainly come from
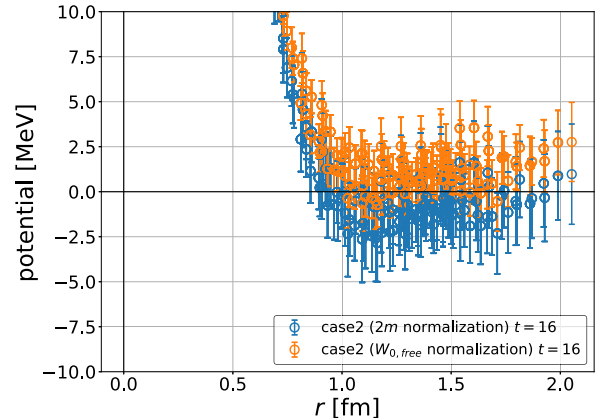
FIG. 9.   A normalization dependence of the potential in the case 1 (left) and the case 2 (right).
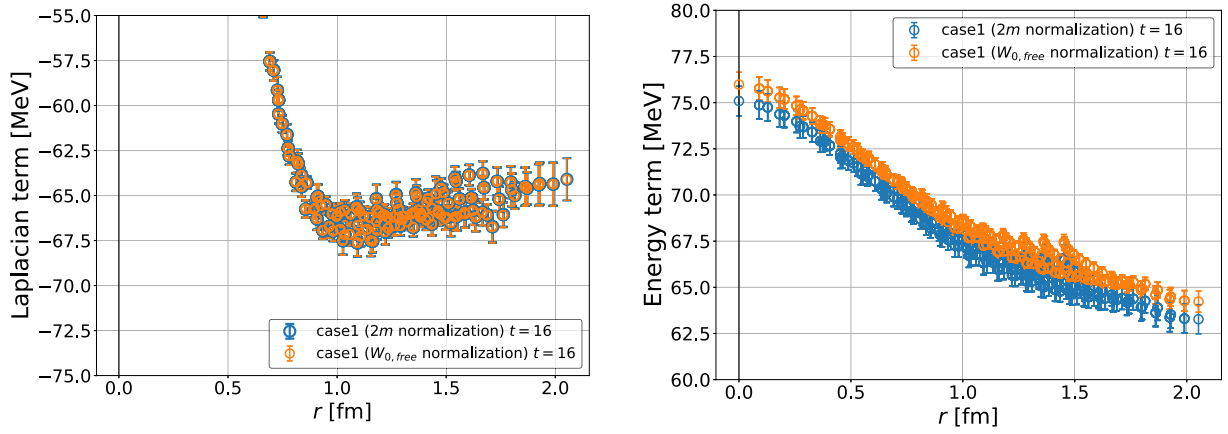
FIG. 10. A normalization dependence of the Laplacian term (left) and the energy term (right) in the case 1.
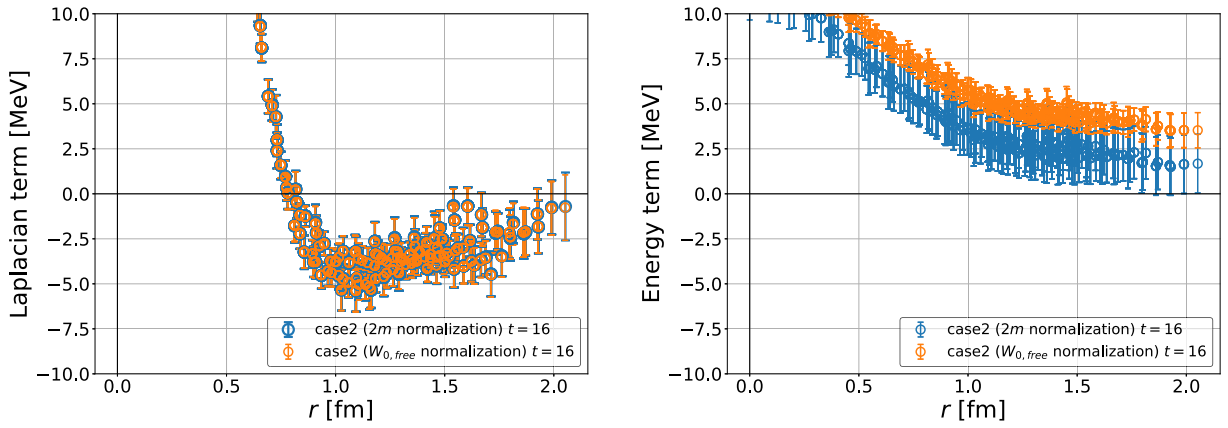
FIG. 11. A normalization dependence of the Laplacian term (left) and the energy term (right) in the case 2.

the energy term, as seen in Figs. 10 and 11. Since an implicit estimation of k_m^2 in the energy term, (35) or (A4), relies on the continuum dispersion relation and involves a discretized second time derivative $\partial_{X_4}^2$, we suspect that

these shifts are caused by finite lattice spacing effects for a larger energy of moving particles and thus, are regarded as discretization errors associated with laboratory frame calculations.
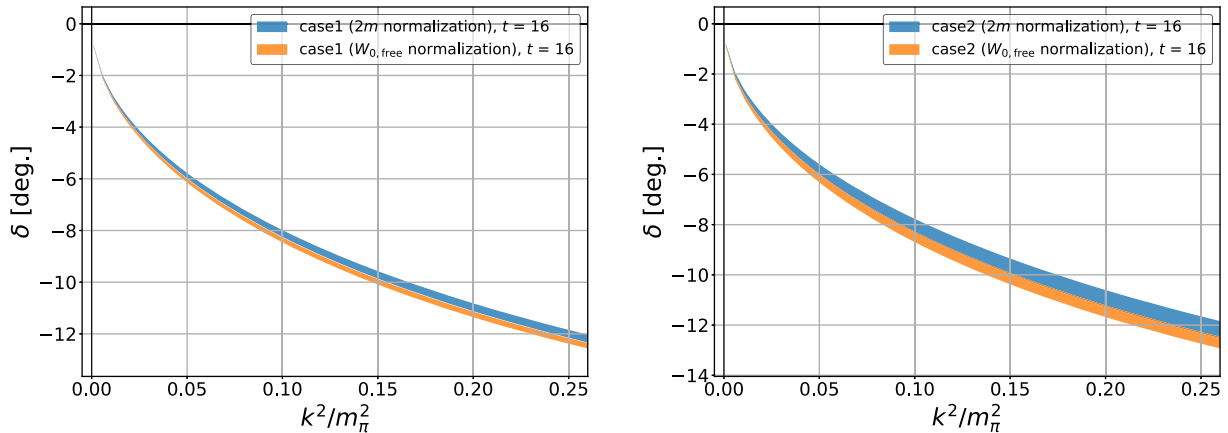
FIG. 12. A normalization dependence of scattering phase shifts at $X^4 = 16$ in the case 1 (left) and the case 2 (right).

Since potentials should become zero at long distances and indeed are consistent with zero within statistical errors, we exclude data at such longer distances and employ data at $r < 13(1.17[\text{fm}])$ for the fit of potentials, (44), in order to reduce statistical and systematic fluctuations of potentials at longer distances as much as possible.
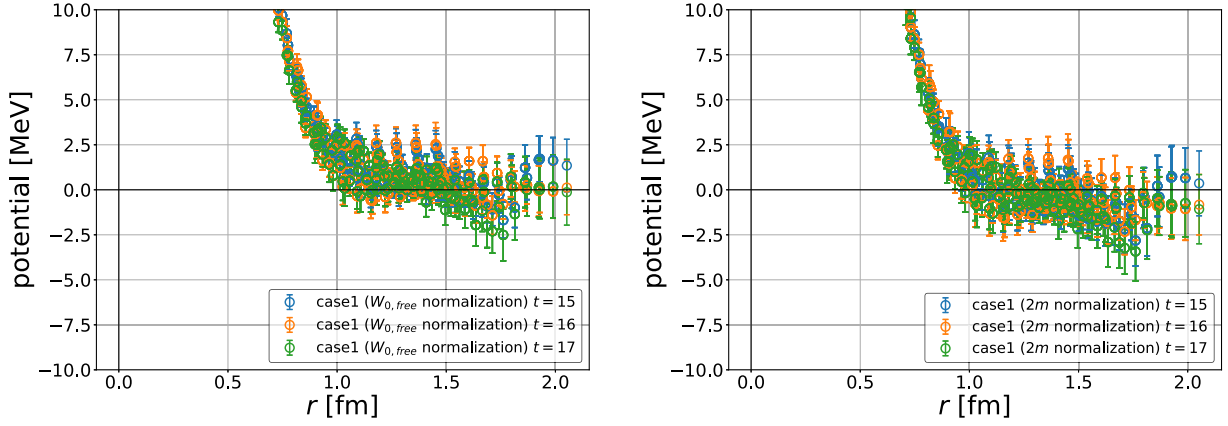
FIG. 13. The X^4 dependence of potentials using $W_{0,\text{free}}$ normalization (left) and $2m$ normalization (right) in the case 1.
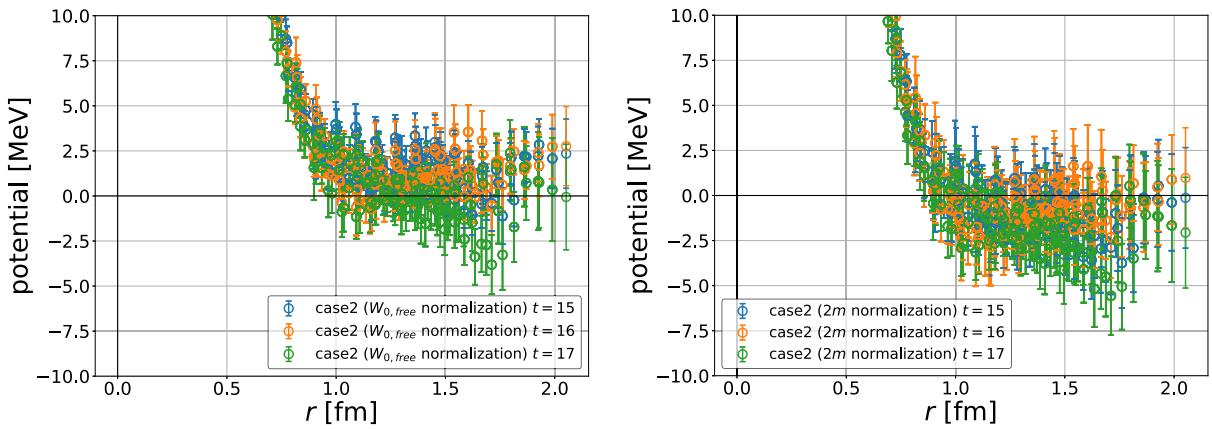
FIG. 14. Same as Fig. 13 in the case 2.
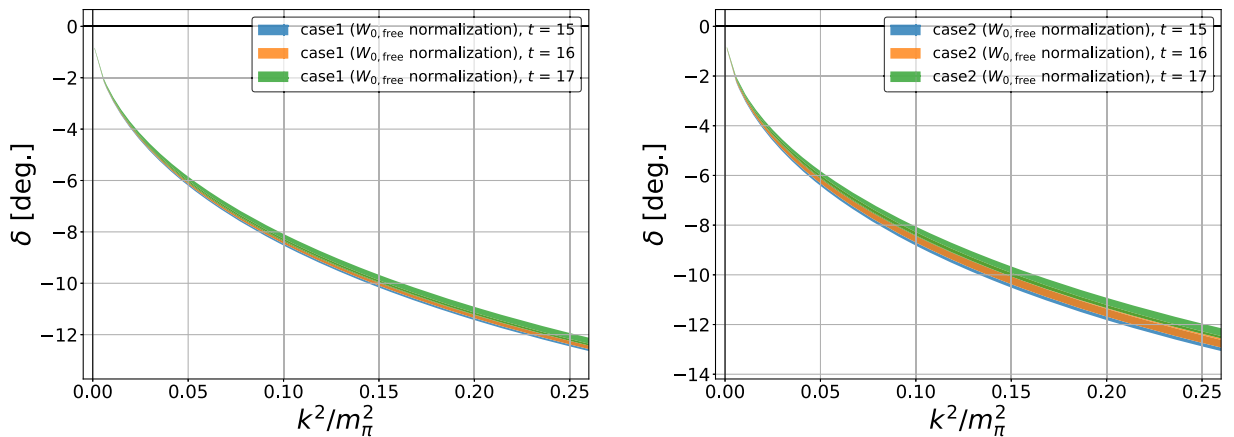
FIG. 15. The X^4 dependence of scattering phase shifts using $W_{0,\text{free}}$ normalization in the case 1 (left) and the case 2 (right). A very similar X^4 dependence is observed in the case of $2m$ normalization.
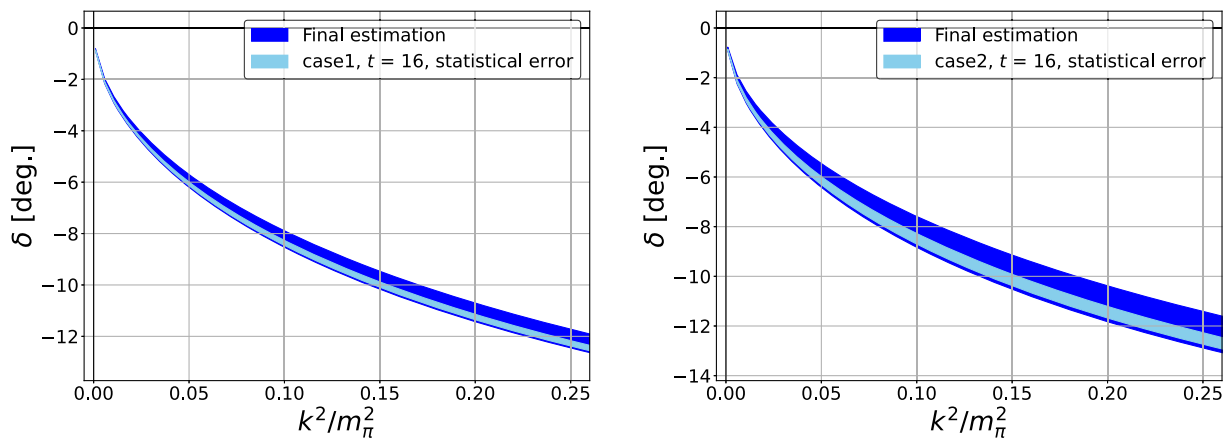
FIG. 16. Scattering phase shifts with the final estimation of uncertainties in the case 1 (left) and the case 2 (right). Blue bands include both statistical and systematic errors added linearly. Light color bands show phase shifts using $W_{0,\text{free}}$ normalization at $X^4 = 16$ that only consider the statistical error.

Figure 12 shows scattering phase shifts as a function of k^2/m_π^2 in two normalizations. We observe a slight difference between the two, which is therefore taken into account for our estimation of systematic uncertainties.

2. Time dependence

We next discuss the X^4 dependence. Figures 13 (case 1) and 14 (case 2) show effective LO potentials at $X^4 = 16 \pm 1$ with nonzero total moment using $W_{0,\text{free}}$ normalization (left) and $2m$ normalization (right). While potentials at different X^4 are statistically consistent with each other, statistical fluctuations of central values slightly affect fit results of potentials. As a result, scattering phase shifts also show a weak dependence on X_4, as seen in Fig. 15 for the

$W_{0,\text{free}}$ normalization. We thus include the X_4 dependence in our estimation of systematic errors.

3. Final estimation of uncertainties

Let us present our final estimation of systematic uncertainties, including both normalization dependence and X^4 dependence of scattering phase shifts. We estimate systematic uncertainties from differences between maximum and minimum of all data at a given energy. Figure 16 shows scattering phase shifts as a function of k^2/m_π^2 with the final estimation of systematic uncertainties, where color bands include both statistical and systematic errors. In the main text, we discuss consistency among different extractions of scattering phase shifts, taking these systematic uncertainties into account.

[1] M. Luscher, Nucl. Phys. **B354**, 531 (1991).
[2] K. Rummukainen and S. A. Gottlieb, Nucl. Phys. **B450**, 397 (1995).
[3] M. T. Hansen and S. R. Sharpe, Phys. Rev. D **86**, 016007 (2012).
[4] N. Ishii, S. Aoki, and T. Hatsuda, Phys. Rev. Lett. **99**, 022001 (2007).
[5] S. Aoki, T. Hatsuda, and N. Ishii, Prog. Theor. Phys. **123**, 89 (2010).
[6] S. Aoki (HAL QCD Collaboration), Prog. Part. Nucl. Phys. **66**, 687 (2011).
[7] N. Ishii, S. Aoki, T. Doi, T. Hatsuda, Y. Ikeda, T. Inoue, K. Murano, H. Nemura, and K. Sasaki (HAL QCD Collaboration), Phys. Lett. B **712**, 437 (2012).
[8] S. Aoki, N. Ishii, T. Doi, T. Hatsuda, Y. Ikeda, T. Inoue, K. Murano, H. Nemura, and K. Sasaki (HAL QCD Collaboration), Proc. Jpn. Acad. Ser. B **87**, 509 (2011).

[9] S. Aoki and T. Doi, Front. Phys. **8**, 307 (2020).
[10] D. Kawai, S. Aoki, T. Doi, Y. Ikeda, T. Inoue, T. Iritani, N. Ishii, T. Miyamoto, H. Nemura, and K. Sasaki (HAL QCD Collaboration), Prog. Theor. Exp. Phys. **2018**, 043B04 (2018).
[11] D. Kawai (HAL QCD Collaboration), EPJ Web Conf. **175**, 05007 (2018).
[12] Y. Akahoshi, S. Aoki, T. Aoyama, T. Doi, T. Miyamoto, and K. Sasaki, Prog. Theor. Exp. Phys. **2020**, 073B07 (2020).
[13] Y. Akahoshi, S. Aoki, T. Aoyama, T. Doi, T. Miyamoto, and K. Sasaki, Prog. Theor. Exp. Phys. **2019**, 083B02 (2019).
[14] R. A. Briceno, J. J. Dudek, and R. D. Young, Rev. Mod. Phys. **90**, 025001 (2018).
[15] M. Mai, U.-G. Meißner, and C. Urbach, Phys. Rep. **1001**, 1 (2023).
[16] Y. Akahoshi, S. Aoki, and T. Doi, Phys. Rev. D **104**, 054510 (2021).

[17] S. Aoki, Proc. Sci. LATTICE2019 (**2019**) 020.
[18] R. Gupta, A. Patel, and S. R. Sharpe, Phys. Rev. D **48**, 388 (1993).
[19] T. Yamazaki *et al.* (*CP*-PACS Collaboration), Phys. Rev. D **70**, 074513 (2004).
[20] S. R. Beane, P. F. Bedaque, K. Orginos, and M. J. Savage (NPLQCD Collaboration), Phys. Rev. D **73**, 054503 (2006).
[21] X. Feng, K. Jansen, and D. B. Renner, Phys. Lett. B **684**, 268 (2010).
[22] J. J. Dudek, R. G. Edwards, and C. E. Thomas, Phys. Rev. D **86**, 034031 (2012).
[23] Z. Fu, Phys. Rev. D **87**, 074501 (2013).
[24] K. Sasaki, N. Ishizuka, M. Oka, and T. Yamazaki (PACS-CS Collaboration), Phys. Rev. D **89**, 054502 (2014).
[25] C. Culver, M. Mai, A. Alexandru, M. Döring, and F. X. Lee, Phys. Rev. D **100**, 034509 (2019).
[26] S. Aoki and Y. Akahoshi, Proc. Sci. LATTICE2021 (**2022**) 546.
[27] S. Aoki, N. Ishii, T. Doi, Y. Ikeda, and T. Inoue, Phys. Rev. D **88**, 014036 (2013).
[28] S. Aoki, T. Doi, T. Hatsuda, Y. Ikeda, T. Inoue, N. Ishii, K. Murano, H. Nemura, and K. Sasaki (HAL QCD Collaboration), Prog. Theor. Exp. Phys. **2012**, 01A105 (2012).

[29] C. McNeile and C. Michael (UKQCD Collaboration), Phys. Rev. D **73**, 074506 (2006).
[30] S. Aoki *et al.* (PACS-CS Collaboration), Phys. Rev. D **79**, 034503 (2009).
[31] Y. Iwasaki, Nucl. Phys. **B258**, 141 (1985).
[32] B. Sheikholeslami and R. Wohlert, Nucl. Phys. **B259**, 572 (1985).
[33] T. Iritani *et al.*, J. High Energy Phys. 10 (2016) 101.
[34] J. Foley, K. Jimmy Juge, A. O'Cais, M. Peardon, S. M. Ryan, and J.-I. Skullerud, Comput. Phys. Commun. **172**, 145 (2005).
[35] T. Miyamoto, Y. Akahoshi, S. Aoki, T. Aoyama, T. Doi, S. Gongyo, and K. Sasaki, Phys. Rev. D **101**, 074514 (2020).
[36] T. Amagasa, S. Aoki, Y. Aoki, T. Aoyama, T. Doi, K. Fukumura, N. Ishii, K. I. Ishikawa, H. Jitsumoto, and H. Kamano *et al.*, J. Phys. Conf. Ser. **664**, 042058 (2015).
[37] S. Ueda, S. Aoki, T. Aoyama, K. Kanaya, H. Matsufuru, S. Motoki, Y. Namekawa, H. Nemura, Y. Taniguchi, and N. Ukita, J. Phys. Conf. Ser. **523**, 012046 (2014).
[38] I. Kanamori and H. Matsufuru, Lect. Notes Comput. Sci. **10962**, 456 (2018).